

UNSTEADY AERODYNAMICS OF SINGLE AND MULTI-ELEMENT AIRFOILS

Loren Ahaus
Post-Doctoral Research Associate
laa1@cec.wustl.edu

Nicholas Liggett
Graduate Research Assistant
Nicholas.Liggett@gatech.edu

David A. Peters
McDonnell Douglas Professor of Engineering
dap@me.wustl.edu
Dep. of Mechanical and Aerospace Engg.
Washington Univ., St. Louis, MO USA

Marilyn J. Smith
Associate Professor
marilyn.smith@ae.gatech.edu
School of Aerospace Engg.
Georgia Inst. of Tech., Atlanta, GA USA

Abstract

Advanced concepts such as active rotor control via dynamic camber, flaps, leading edge slats and other methods have transformative research potential to improve rotorcraft vibration and performance, as well as to reduce rotor noise. Dynamic stall on the retreating side of the rotor needs to be captured and minimized, and the influence of gaps between the multiple elements of the rotor must be understood. Computational fluid dynamics (CFD) methods using advanced turbulence modeling techniques, in conjunction with experimental results, are used to increase the understanding of the physics of these gaps for static and dynamic stall conditions. These results are also used to aid in the development of unsteady unified aerodynamics theory (UAT), in particular, drag predictions, necessary for design and rapid analysis of these advanced concepts. Initial analysis of the influence of wind tunnel walls on static and dynamic single and multi-element airfoils is also included. Good correlation is seen with the new UAT drag prediction and CFD predictions for the multi-element airfoil, closing the gap where experimental data are not available.

INTRODUCTION

Helicopter rotor blades, unlike their fixed wing counterparts, frequently encounter dynamic stall during normal flight conditions, limiting the applicability of classical thin airfoil theory at large angles of attack. Dynamic stall is a complicated aerodynamic phenomenon in which a vortex-like disturbance is shed by the two- or three-dimensional configuration at large angles of attack. The disturbances may originate at either the leading or trailing edge and translate along the airfoil, resulting in highly non-linear pressure disturbances. This nonlinearity causes the airloads to diverge significantly from those efficiently predicted by linear, thin-airfoil theory.

In part to alleviate the negative influences of dynamic stall, active control concepts including dynamic camber, flaps, and leading edge slats are under investigation to improve rotorcraft vibration and performance, as well as to reduce noise. Experimental campaigns with flapped wings and airfoils have been carried out to investigate their role in improving the performance of wings and rotors [3–7, 9]. Greenwell [3] studied trailing edge gurney flaps, noting that while flap deployment leads to an increase in the profile drag, it can be counteracted by reduction in the induced drag. Additional research by Maughmer [5] confirmed the importance of scheduling frequency and chordwise flap placement. Krzysiak and Narkiewicz [6] have examined dynamic airfoil and flap configurations where each element deflects sinusoidally at different rates and phases. Their two-dimensional, inviscid, incompressible model applied to the test configurations demon-

NOMENCLATURE

a	speed of sound, $\frac{ft}{sec}$
b	rotor blade semichord, ft
c	rotor blade chord length, ft
C_d	sectional drag coefficient
C_l	sectional lift coefficient
C_m	sectional pitching moment coefficient
e	stall parameter for UAT
L_n	generalized load per unit length, lbs/ft
M	Mach number
Re	Reynolds number
x, y, z	Cartesian streamwise, radial and normal lengths, ft
V	velocity, $\frac{ft}{sec}$
y^+	dimensionless wall spacing
α	angle of attack, $^\circ$
Γ_n	generalized circulation change, $\frac{ft^2}{s}$
δ	deflection angle of flap, $^\circ$
ΔC_n	static residual of the n th load
η	stall parameter for UAT
ρ	air density, $\frac{slugs}{ft^3}$
ϕ	phase lag between pitch and flap motions, $^\circ$
ω	stall parameter for UAT

strated adequate performance in the linear regime, but, as expected, did not correlate well with experiment in the stalled region. With an aim of improving performance, Kiedaisch [4] tested static high lift wings in two-dimensional and three-dimensional configurations with multiple geometries, including trailing edge flaps and leading edge droop with a focus on active flow control (AFC). His work provides insight to the physics of the element type that is employed. Larger increments in lift were obtained from AFC combined with vented or slotted flaps than with simple flaps. Novel methods for improved characteristics have also been investigated by Little [9], where a plasma discharge actuator placed at the flap shoulder of a NASA Energy Efficient Transport airfoil delayed separation. Operation of the actuator in an unsteady fashion at the natural frequency of the trailing edge flow served to enhance the natural instabilities in the flowfield and energized the boundary layer, with the eventual result of giving higher lift. Dynamic trailing edge flaps with independently dynamic leading edge deformation were considered by Lee [7] with the goal of alleviating dynamic stall vortex shedding. The lift augmentation from the trailing edge flap was further aided by the leading edge deflection, but the issues with dynamic testing were noted, as parametric studies varying scheduling were needed, but not available, for additional support.

There have been many semi-empirical models designed to quantify the effect of dynamic stall on airloads [12]. The models, usually based on wind tunnel testing, are typically applied as empirical corrections to steady data and are restricted to the range of airfoil types, angle of attack, Mach number, etc. from which they were derived. ONERA developed a third-order model of dynamic stall [18, 19], which has been validated via a fairly extensive wind tunnel test program at the NASA Ames research facility [11]. While the model is unable to reproduce some of the severe overshoot associated with certain dynamic stall scenarios, it does capture the character of the stall. Its ease of incorporation into any airloads theory makes it an attractive model for handling dynamic stall.

These models have been based on single-element rigid airfoils, which limits their application for many active control techniques under development. CFD simulations have been applied almost exclusively to model the flow about multi-element geometries [for example Refs. 15 and 17]. While CFD predictions have agreed with experimental data at lower angles of attack, the maximum lift coefficient is overpredicted and the onset of stall is missed, even in many cases when transition is modeled. Zhang [23] combined a two-dimensional RANS solver in the steady, attached region of the airfoil upstream of the flap and in the far-field and a Large-Eddy Simulation (LES) to resolve the region surrounding the flap. Reductions of 50% in terms of computational resources were achieved while maintaining qualitative agreement with a full LES solution. Liu et al. [10] conducted a study using two RANS solvers, one of which incorporated an LES based turbulence technique, to study actively controlled trailing edge flaps for used in advanced rotor designs. Vortex shedding due to the presence of the flap gap illuminated the need for high fidelity considerations. Additionally, a reduced order model using Rational Function Approximation trained with the CFD solutions provided unsteady loads on par with the computa-

tional results.

A unified aerodynamics theory (UAT) has been developed by Ahaus and Peters [1, 2] to close the gap between the single element linear theory and CFD. The theory thus far has been demonstrated to successfully predict the lift and moment for a variety of morphed airfoils, and its extension to multi-element airfoils has been initially correlated. This work extends the development of the UAT to further explore dynamic stall of single- and multi-element airfoils, combining experimental and computational results to guide this development. CFD simulations using a hybrid RANS/LES turbulence method are employed to permit an insightful examination of the physics of the flow field and airfoil performance via cross-correlation from each source.

DATA CORRELATION

Data were correlated with both symmetric and cambered airfoils, the NACA0012 and VR-7, respectively. These airfoil test results included static and dynamic integrated loads and moments, which were utilized to help train the stall model and provide guidance for the CFD simulations. The UAT and CFD processes were then applied to the NACA0012 airfoil which included a moving flap.

NACA0012

A large set of experimental data is available for the NACA 0012 airfoil. These data were reviewed in a comprehensive survey by McCroskey [13]. Airfoil characteristics from a wide range of test facilities, including over 40 wind tunnels with various test conditions, were made available through this compilation. Lift-curve slope, maximum lift coefficient, and zero-lift drag coefficient numbers varying over the full transonic regime from 0.1 through 1.2 were documented, as well as variation in Reynolds numbers from 2×10^5 up to 4×10^7 . The Mach 0.5 integrated coefficients provide experimental correlation for this work. Data were sorted into groups by McCroskey based on the fidelity of the experiment. Error tolerances for the group one data, utilized in this effort, were reported to be no greater than ± 0.0040 for the lift data and ± 0.0010 for the drag data. No tolerance for the moment data was specified.

VR-7

A significant endeavour by McCroskey, McAlister, Carr, and Pucci [14] evaluated both static and dynamic data for a variety of airfoils in the atmospheric pressure solid-wall Wind Tunnel at the U.S. Army Aeromechanics Laboratory for studying static and dynamic stall. These tests obtained data for a VR-7 airfoil with a chord of 0.61 of a $2 \text{ m} \times 3 \text{ m}$ wind tunnel. The static data were gathered nominally at a Mach number of 0.185 and a Reynolds number of 2.59 million per chord. Dynamic stall data were collected for Mach numbers of 0.30 and a Reynolds number of 4.2 million per chord.

Pressures at 26 tap locations were averaged over 50 cycles from 200 sets of measurements taken at equal time intervals.

The pressure data is reported to be accurate to within 0.02 psi at angles of attack accurate to within 0.05° . Lift, drag, and moment coefficients were integrated via a trapezoidal scheme. McCroskey et al. noted that the static data may contain wind tunnel wall effects, as determined through comparison of select data with the work of other facilities. Wind tunnel wall contamination and three-dimensional effects were considered to be a relatively small issue for the dynamic data, due to the high aspect ratios and sidewall boundary layer control within the test section. These issues are further addressed in a recent study by Moulton and Smith [16].

NACA 0012 with moving flap

Krzysiak and Narkiewicz have investigated an oscillating NACA 0012 airfoil with an oscillating trailing edge flap [6]. The airfoil had a total chord of 0.18 m and a span of 0.6 m evaluated in a wind tunnel with a cross section of $0.6 \text{ m} \times 0.6 \text{ m}$. The length of the airfoil flap was 0.04069 m with a leading edge radius of 0.00469 m. The gap between the flap and the airfoil was at a minimum 0.0005 m with no gap overhang present. The axes of rotation of the airfoil and flap were at 35% and 80% of the chord, respectively. Static tests starting from a 0° angle of attack maintained a 0° flap deflection angle at a 0.5 Mach number and a Reynolds number of 1.99 million, while dynamic tests had a Mach number of 0.4 and Reynolds number of 1.63 million.

Dynamic stall tests combined airfoil and flap oscillations via prescribed motions defined as:

$$(1) \quad \begin{aligned} \alpha &= \alpha_{mean} + \Delta\alpha * \sin(k_{airfoil} * t) \\ \delta &= \delta_{mean} + \Delta\delta * \sin(k_{flap} * t) \end{aligned}$$

where α is the airfoil angle of attack and δ is the flap deflection angle. Reduced frequencies of $k_{airfoil} = 0.021$ and $k_{flap} = 0.042$ correspond to airfoil and flap sinusoidal oscillations at 5 Hz and 10 Hz, respectively. Two mean airfoil angles of attack were analyzed, $\alpha = 4^\circ$ and 11° with a mean flap deflection $\delta = 0^\circ$. The amplitude of oscillation for all motion ($\Delta\alpha$ and $\Delta\delta$) was 5° . The flap deflection included phase lags of 148° , 206° , and 298° for the $\alpha_{mean} = 4^\circ$ tests, and phase lags of 177° and 343° for the $\alpha_{mean} = 11^\circ$ tests.

Data were obtained using 48 pressure sensors along the mid-span. For the dynamic oscillations, ten cycles of data were averaged with 25 data sets per cycle to obtain the integrated lift and moment coefficients. No pressure drag coefficient data were reported. Instrumentation errors of 0.1° and 0.05% for the angles and pressures, respectively, were reported. Wind tunnel effects were not addressed for either the static or dynamic data.

UNIFIED AERODYNAMICS THEORY

The Unified Aerodynamics Theory (UAT), based on the work of Refs. [1] and [2], consists of three components. Unstalled airloads are calculated by a state-space linear airload theory using an expansion of the airfoil geometry into generalized coordinates. This theory is coupled to an inflow model. Stalled

airloads are computed using an adaptation of the ONERA stall model. This approach filters the stalled airloads dynamically:

$$(2) \quad \frac{b^2}{V^2} \ddot{\Gamma}_n + \eta \frac{b}{V} \dot{\Gamma}_n + \omega^2 \Gamma_n = -bV\omega^2 \left[\Delta C_n + e \frac{d\Delta C_n}{dt} \frac{b}{V} \right]$$

where ΔC_n is the static stall and Γ_n is the dynamic change in circulation of the n th generalized load due to stall. The stall parameters ω , η , and e are identified by training the model through a genetic optimization. Both experimental and CFD data have been used successfully as the reference for training the model. The total generalized loads are computed by:

$$(3) \quad L_n = L_{n(\text{linear})} + \rho V \Gamma_n$$

The UAT also employs an unsteady approximation for drag. Thin-airfoil theory gives only the induced drag, which must be combined with the profile drag to determine the total drag. The unstalled profile drag is generally proportional to a constant plus a term proportional to α^2 . Thus, a parabola can be fit to the supplied drag data (from experiment or CFD) in the unstalled region, defining the unstalled profile drag. The parabolic profile drag is treated as quasi-steady. The increment in drag due to stall beyond the parabolic shape is then defined by:

$$(4) \quad \Delta C_d = C_{d(\text{exp.})} - C_{d(\text{parabolic})}$$

The drag residual is processed through a dynamic filter, similar to that shown in Eq. (2). Finally, the total dynamic drag is the sum of the quasi-steady parabolic drag, the unsteady drag due to dynamic stall, and the induced drag from the thin-airfoil theory.

$$(5) \quad C_{d(\text{total})} = C_{d(\text{induced})} + C_{d(\text{parabolic})} + \frac{\Gamma_d}{bV}$$

CFD SIMULATIONS

CFD Methodology

The CFD simulations have been obtained via the OVERFLOW 2.1z code, using advanced turbulence models based on hybrid RANS-LES [8, 20, 21]. For the static NACA 0012 simulations, a time step of 7.8×10^{-5} seconds is used. For the dynamic NACA 0012 simulations, a time step of 4.85×10^{-5} seconds provides 4,000 iterations per oscillation cycle. The lower speed VR-7 data was simulated with a time step of 7.1×10^{-4} seconds for the static runs and 4.8×10^{-5} seconds for the dynamic case providing 6,000 iterations per oscillation cycle. These time steps are combined with an ARC3D diagonalized Beam-Warming scalar pentadiagonal scheme and 20 2^{nd} -order accurate Newton sub-iterations for the temporal integration. A 4^{th} -order spatial discretization formulation is employed with central difference Euler terms and a generalized thin-layer Navier-Stokes (TLNS3D) dissipation scheme, which adds smoothing to the 2^{nd} and 4^{th} -order ρh_0 discretization terms in the form of dissipation coefficients. The coefficients are 2.0 and 0.04 for these discretization terms, respectively.

Six different three-dimensional grids have been used for static and dynamic simulations. Meshes for the NACA 0012, flapped NACA 0012, and VR-7 airfoils have been evaluated. Each configuration was simulated for both a wind tunnel grid and in free air to ascertain the effect of wind tunnel walls on the results. These simulations employ an over-set method, which allows a combination of body-fitted and far field meshes to be used with interpolation of the field variables at the overlaps. Previous grid studies [22] for airfoil configurations ranging from steady and attached to highly stalled (approaching flat plate behavior) flow provided guidance in the grid development, and acted as a grid study for this effort. Initial normal spacing on viscous surfaces ensured that $y^+ < 1$ for all configurations. All three-dimensional simulations included at least 15 nodes per chord radial length, as indicated by prior studies to minimize grid dependence. The wind tunnel walls were modeled using inviscid wall boundary conditions.

NACA 0012: The grid configuration for the NACA 0012 airfoil in the wind tunnel is outlined in Fig. 1. Wind tunnel background, near-body airfoil, and refined wake grids provided unsteady wake resolution. The wind tunnel grid included 475 points in the streamwise and 141 points in the normal coordinate system, and the refined wake grid was comprised of 204 nodes in the streamwise and 181 node for the normal axes. The NACA 0012 profile was modeled with a finite-thickness trailing edge via an O-grid topology. The airfoil near-body grid, shown in Fig. 2, included 971 nodes in the circumferential direction and 120 nodes in the surface normal direction, with the outer boundary extending about 2.0 chords from the surface.

The complementary free air background mesh employed 200 nodes in the normal direction for the outer boundary located 30 chords from the airfoil surface, but maintained the mesh structure of the background grid in the other directions.

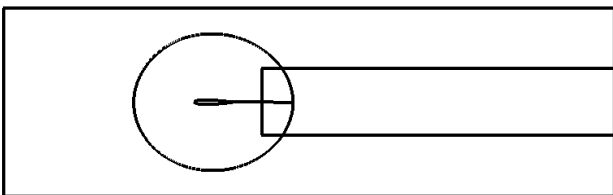
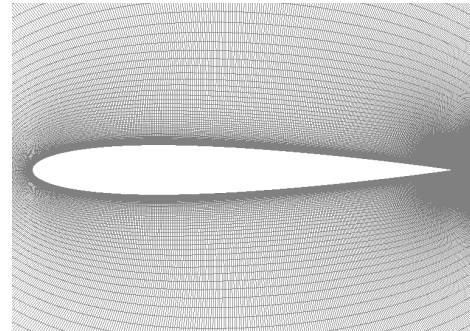


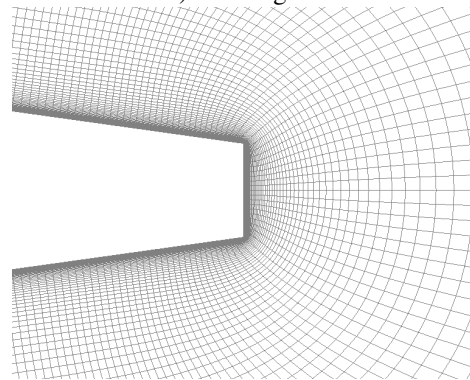
Figure 1: NACA 0012 airfoil wind tunnel grid system.

Flapped NACA 0012: The flapped NACA 0012 configuration incorporated 4 grids: a wind tunnel grid, an airfoil body O-grid, a flap C-grid with wake refinement, and a patch grid for the C-grid boundary condition. The background mesh was 286 points in the streamwise and 173 points in the normal directions. The airfoil and flap meshes contain 374 and 400 streamwise points, respectively, where 75 nodes in the flap grid extend into the near wake to provide a refined grid. Both grids incorporate 200 nodes in the direction normal to the surface, and extend outward by 1.5 and 1.25 chords, respectively. The complementary free air background mesh again employed 200 nodes in the normal direction for the outer boundary.

VR-7: A similar approach to the NACA 0012 grid system was employed for the VR-7 wind tunnel case. The VR-7 airfoil (Fig. 4) also utilized an O-grid topology due to the blunted trailing edge and tab. It included 811 points in the streamwise axis, with 459 points on the upper surface. The near-body mesh extends outward 2 chords with 200 nodes.

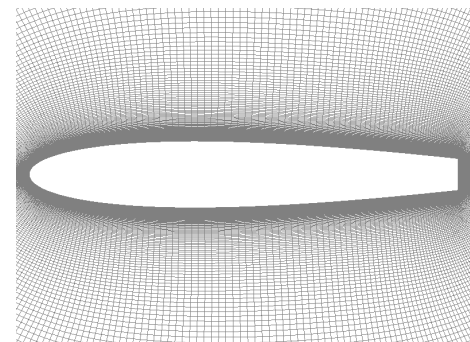


a) Airfoil grid.

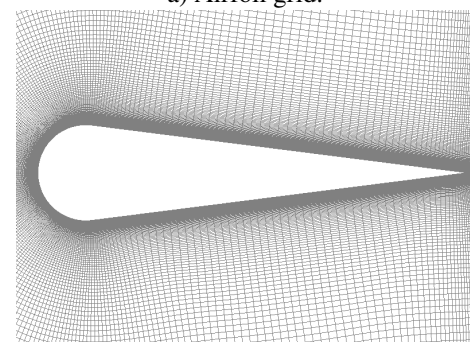


b) Close-up of trailing edge.

Figure 2: NACA 0012 airfoil O-grid.



a) Airfoil grid.



b) Flap grid.

Figure 3: Flapped NACA 0012 airfoil grid.

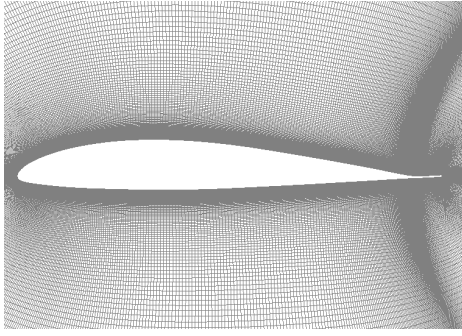


Figure 4: VR-7 airfoil grid with trailing edge tab.

RESULTS

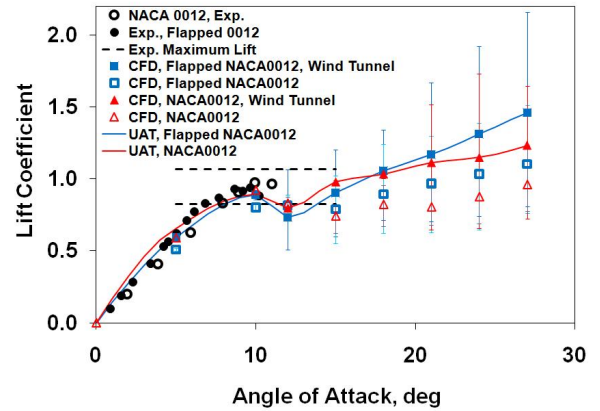
Static Airfoil Evaluation

An advantage of the UAT model is the ease with which linear airloads and stalled airloads are separated. Correction factors within the linear portion of the theory allow the user to match available experimental data for the slopes and intercepts of the airloads. The stalled airloads are affected by the *difference* between these corrected linear loads and the experimental data. The primary concern is capturing the correct post-stall behavior of ΔC_l , ΔC_m , and ΔC_d . For instance, Fig. 5 includes the static lift coefficient data of the NACA0012 airfoil. The change in slope and intercept of the lift curve can be accounted for with correction factors within the linear theory. Figure 6 shows the lift residuals, ΔC_l , plotted for the same data. From this figure, the post-stall behavior is evident. This separation of linear and stalled airloads improves the robustness of the model and makes it less sensitive to the static data used for training.

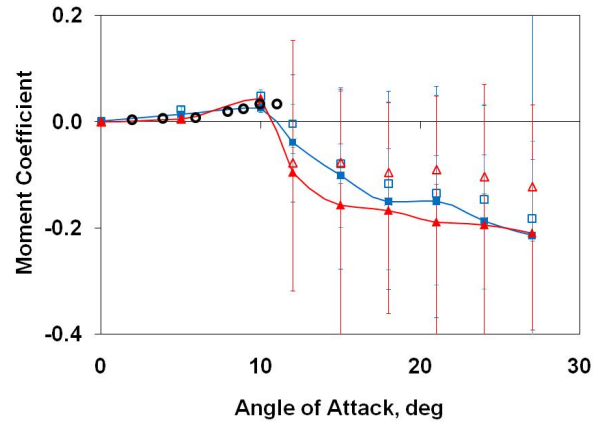
Relatively small differences between the free air and wind tunnel integrated coefficients become more apparent after the airfoil stalls as observed in Fig. 5. The presence of the wind tunnel walls induces an approximately constant increase in lift, negative increase in moment, and increase in drag over the prediction with unconstrained outer boundaries. This shift is observed for both the NACA0012 airfoil and its counterpart with 20% flaps, and except for the moment, the deltas are approximately equal in magnitude. These differences can be readily explained via changes in the airfoil pressure coefficient in pre- and post-stall angles of attack (Fig. 7). The wind tunnel walls restrict the flow and result in a higher suction peak compared to its counterpart, concluding in the expected behaviors observed in the integrated loads. In the post-stall region, separation occurs earlier in the configuration modeled with the wind tunnel walls. This behavior is typical, and gives rise to wall corrections that adjust the angle of attack. The stall reproduced by the simulations fall within the experimental stall limits, plotted as dashed lines on the lift curve. Additionally, the predicted linear slopes of the lift are 0.120 and 0.103 per degree, respectively, for the wind tunnel and free air data. These lie between the experimental limits of 0.109 and 0.138 per degree at the given Mach number.

At angles of attack below stall, the flow is steady and attached, so that the influence of the gap is minimized. The flow through the gap is minimal until angles of attack of 20° or higher are

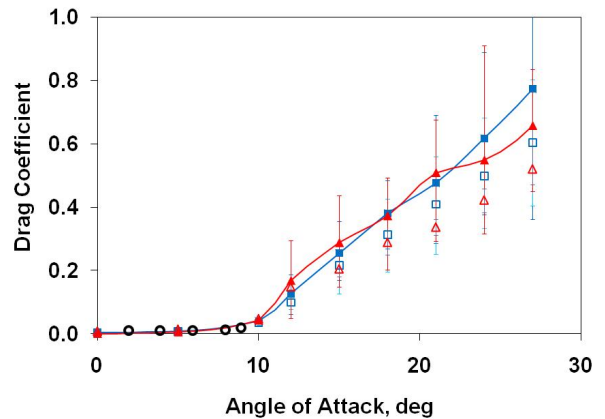
encountered. The resulting pressure discontinuities in the gap region result in an increase in lift due to suction, but also an increase in drag. As the angle of attack increases further, more of the gap is directly exposed to the free stream flow, which increases these differences in integrated forces and moments.



a) Lift coefficient



b) Moment coefficient



c) Drag coefficient

Figure 5: Static coefficient predictions for a NACA0012 airfoil and a NACA0012 airfoil with a 20% flap.

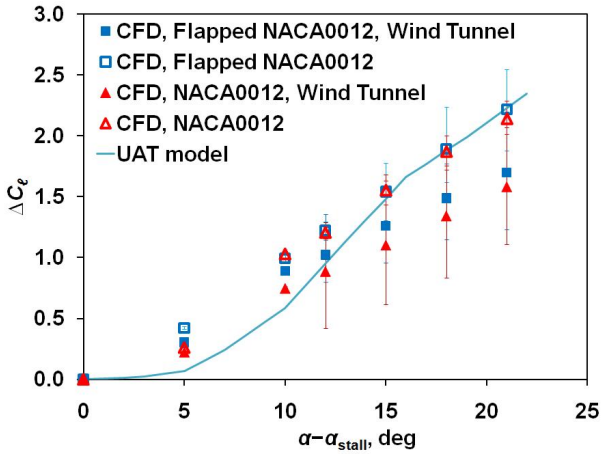
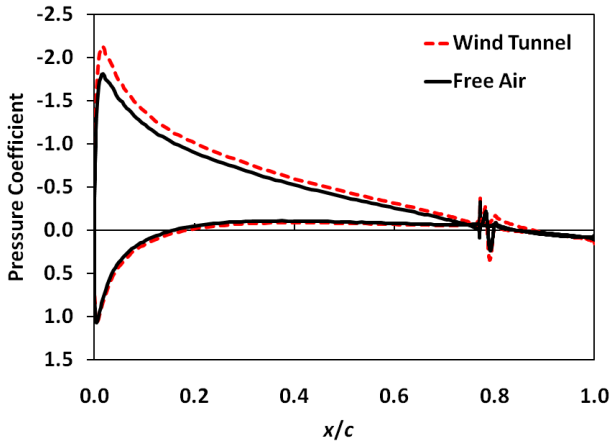
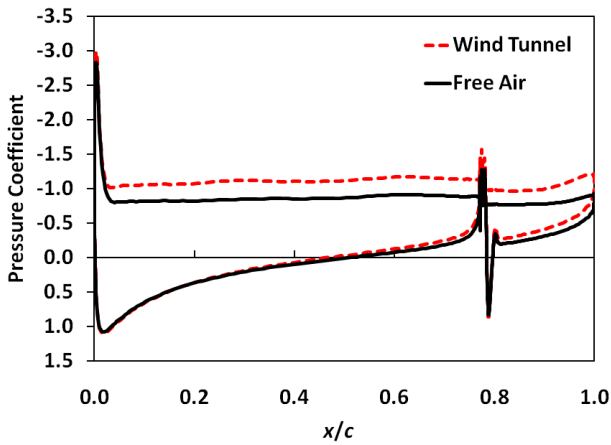


Figure 6: Static lift residual for NACA0012 airfoil.



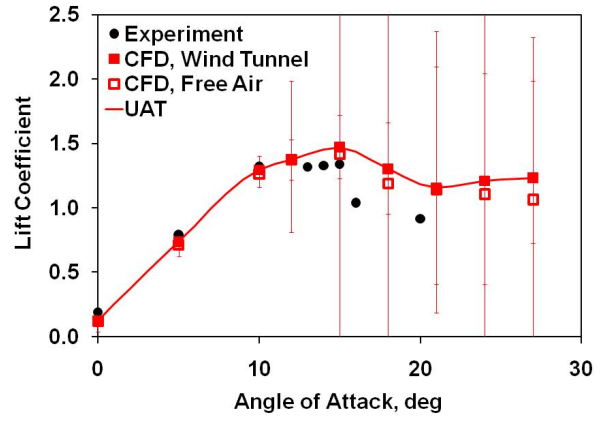
a) Pre-stall, $\alpha = 5^\circ$



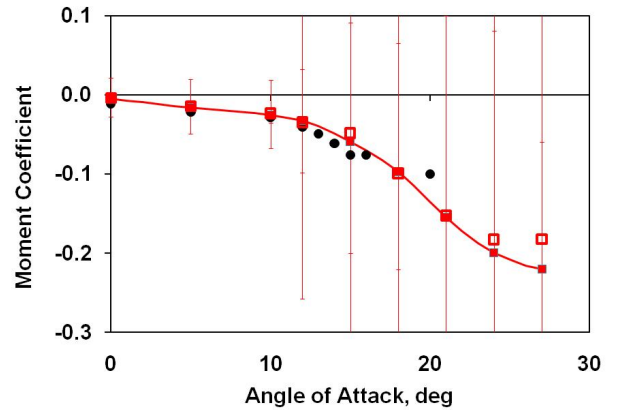
b) Post-stall, $\alpha = 18^\circ$

Figure 7: Static surface pressure coefficients for the flapped NACA 0012 airfoil.

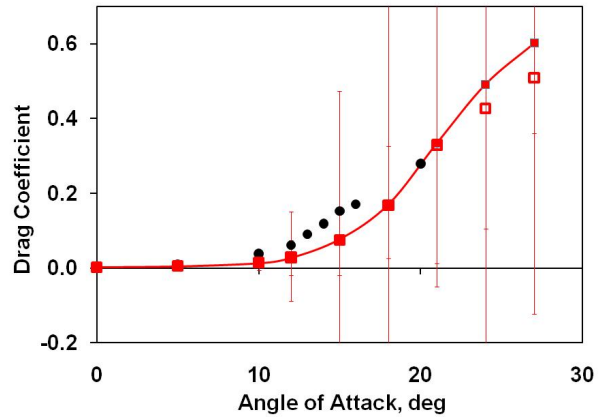
The location of separation is likewise influenced by the presence of the wind tunnel walls and the gap. The addition of the flap causes the separation point shift further aft on the chord. This shift can be almost entirely negated when the simulation is confined within the inviscid boundary conditions of the wind tunnel.



a) Lift coefficient



b) Moment coefficient



c) Drag coefficient

Figure 8: Static coefficient predictions for a VR-7 airfoil.

The thicker VR-7 airfoil has more gentle stall characteristics (Fig. 8), leading to a slower drop in lift with respect to angle of attack as compared with the thinner NACA0012 airfoil. Blockage effects are not as significant as the NACA0012 airfoil, due to the different experimental setup.

Dynamic Single-element Airfoil

The extensive experimental effort by Ref. 11 included an investigation of the cambered VR-7 airfoil. Figure 9 shows the lift, pitching moment, and drag for this airfoil oscillating with $\alpha_{mean} = 15^\circ$ and $\Delta\alpha = 10^\circ$ for a reduced frequency of $k = 0.1$ and Mach number 0.184. This case is of particular interest,

because it illustrates the existence of a double dynamic stall peak.

Vorticity flowfields highlight this phenomenon (Fig. 10). After the initial separation near the leading edge, a secondary separation occurs near the trailing edge. This accounts for the initial stall at about 21° , followed by a slight recovery, which then stalls again near 23° . The strong recirculating flow accompanying the loss in lift is visible in the vorticity plots at $\alpha = 24.14^\circ$. This double stall behavior leads to a two-part recovery as well. The buildup of a sheet of vorticity at 24.84° on the upper surface of the airfoil prevents the initial recovery, after which a strong transient suction is present at $\alpha = 24.29^\circ$. The shedding of this upper layer of vorticity then coincides with the large loss in lift as the angle of attack decreases below 24° . The CFD model is able to capture this double stall behavior, both on the upstroke and the downstroke. However, the CFD predicts a slower recovery in the region below 19° . Further investigation into this slow recovery has been undertaken in Moulton and Smith [16]. Small changes in the reduced frequency change the recovery characteristics of this airfoil, as observed in the reduced frequency sweep of Ref. 14. The nominal reduced frequency of $k = 0.1$ appears to be lower than the actual reduced frequency of the simulation [16]. This behavior has been confirmed using another CFD method, grid and turbulence model, and so is not characterized by the CFD technique chosen for this work.

The UAT model was trained to minimize the least-squares error between the experimental data and the model. The resulting dynamic stall parameters had the effect of splitting the difference between the two stall peaks. Thus, due to the simplicity of the UAT model, it is not capable of predicting the double stall peaks. However, the overall correlation is quite reasonable. For future investigations, it may be possible to increase the fidelity of the UAT model with higher-order terms (additional poles and zeros) to allow for better resolution of the double-stall phenomenon.

Dynamic Airfoil with Flaps

Krzysiak and Narkiewicz [6] published equations that described the airfoil and flap motion for a series of combinations (e.g., for the flap, $\delta = \delta_{mean} + \Delta\delta\sin[\omega_{flap}t - \phi]$). It was observed after computing the CFD results that they sometimes had poorer than expected correlation with experiment. Further analysis of the figures in the paper revealed a flap motion that in some instances did not correlate exactly with the published equation, as illustrated in Fig. 11, giving rise to substantial errors. It was also noted by Ref. 6 that torsional deflections resulted in a change in the nominal angle of attack at the higher angles of attack. Thus while the angle of attack is set nominally to ten degrees ($\alpha_{mean} = 10^\circ$), the actual angle of attack was 11° . The actual data were digitized and applied, rather than nominal equations. The significance of the differences between the published equations and actual motion varied between each dynamic stall case found in Krzysiak and Narkiewicz [6], therefore, it is recommended that the actual motion be utilized for simulations.

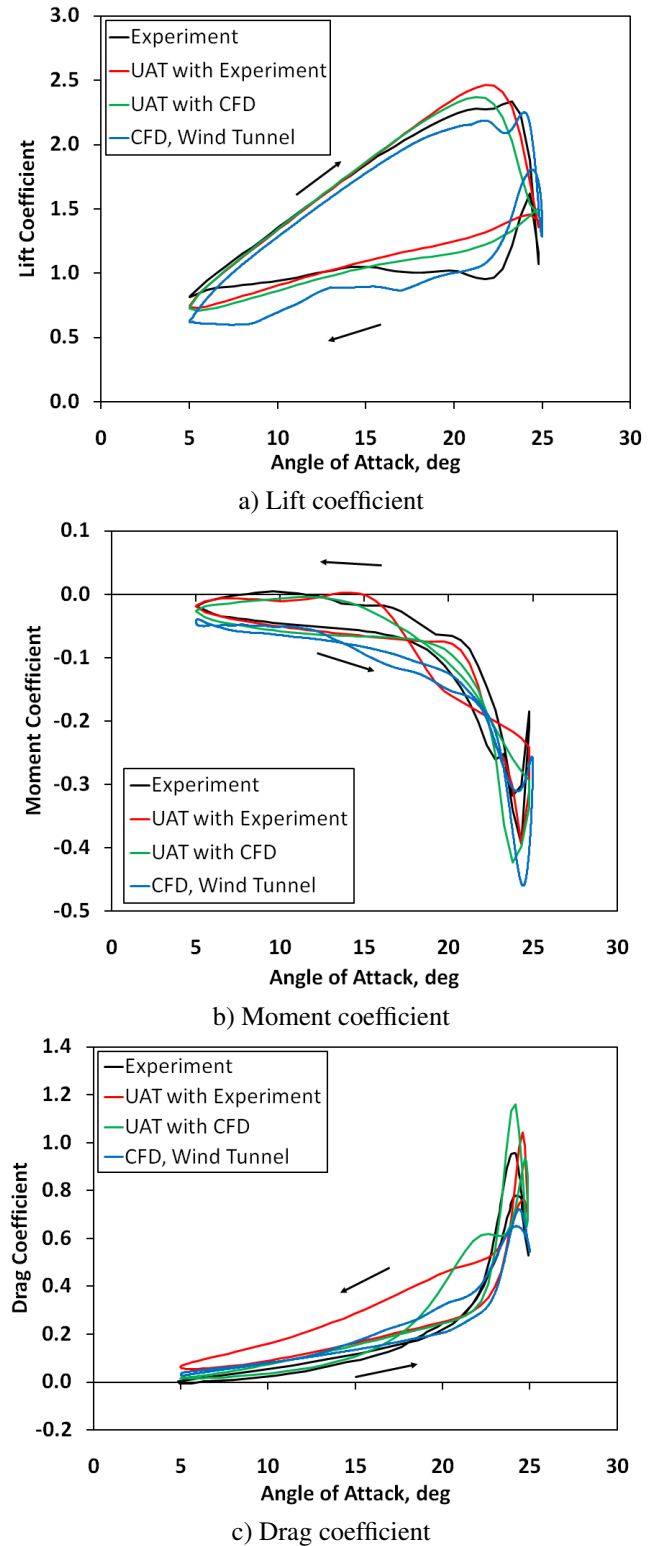
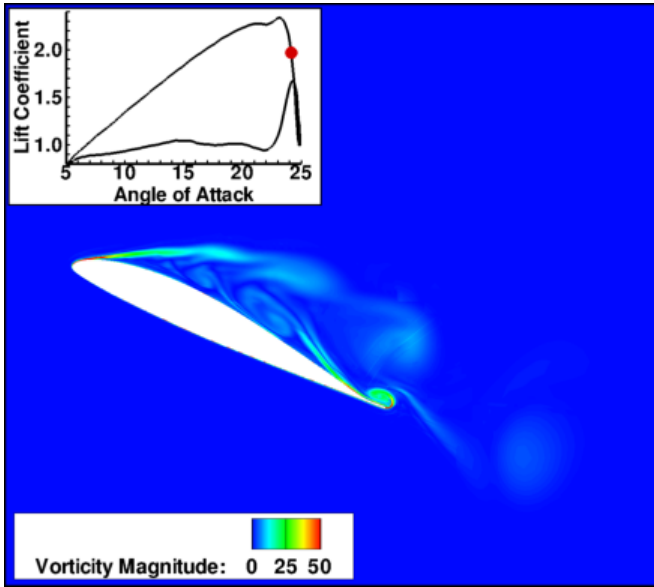
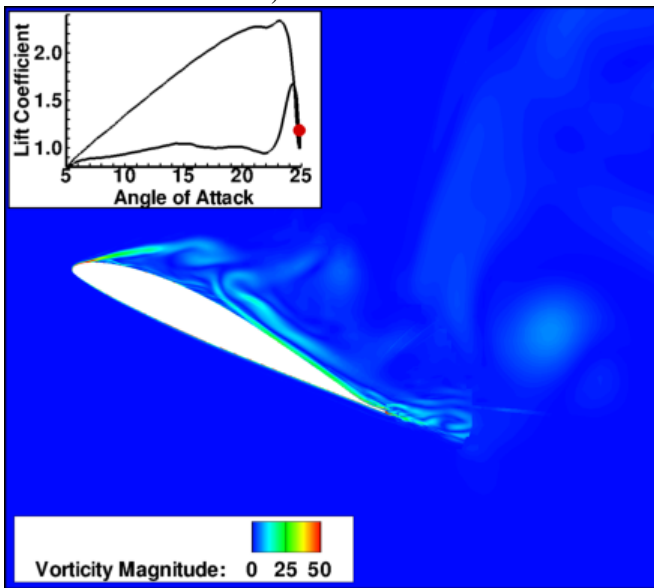


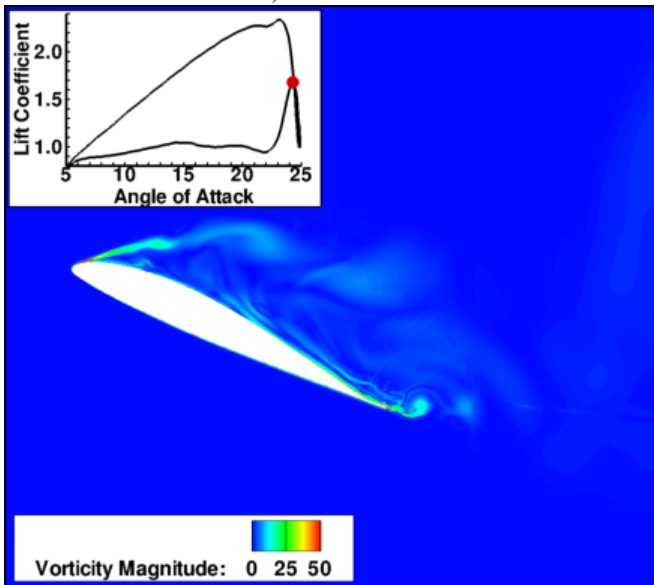
Figure 9: Dynamic coefficients for the VR-7 airfoil for $\alpha_{mean}=15^\circ$, $\Delta\alpha=10^\circ$, $k=0.1$ compared with experimental results [14].



a) $\alpha = 24.14^\circ$

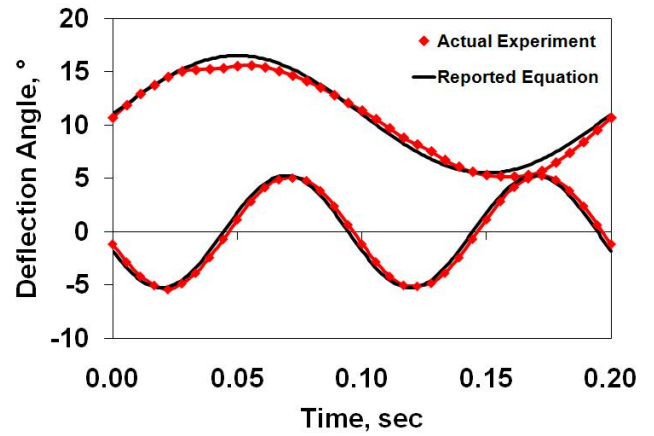


b) $\alpha = 24.84^\circ$

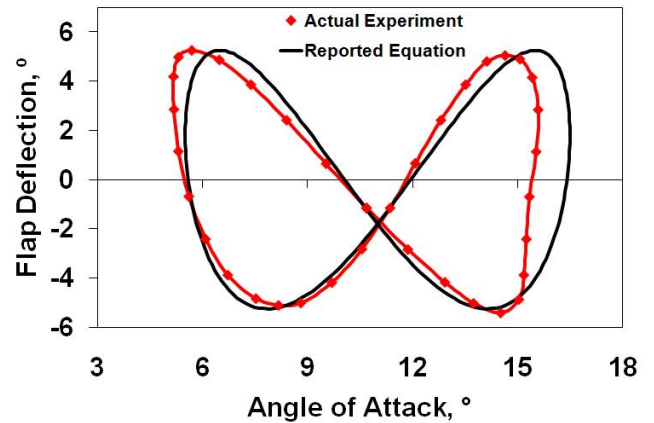


c) $\alpha = 24.29^\circ$

Figure 10: Vorticity flowfield for the VR-7 airfoil for $k = 0.10$ at double stall.



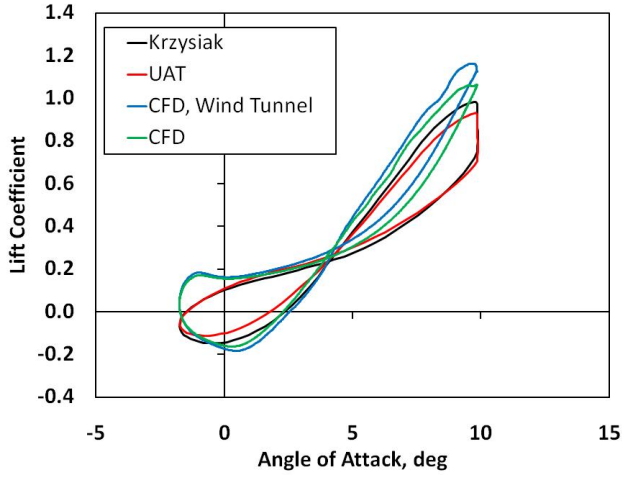
a) Motion over time. Upper curve describes the airfoil motion, while the lower curve describes the flap motion.



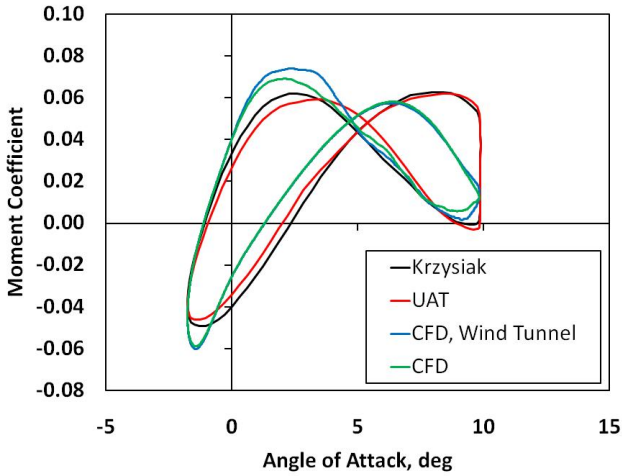
b) Flap deflection scheduling.

Figure 11: An example of a published [6] equation to describe the airfoil ($\alpha = 11^\circ + 5.5^\circ \sin[0.021t]$) and flap motion ($\delta = 0^\circ + 5.25^\circ \sin[0.042t - 160^\circ]$) and actual motions measured during the experiment.

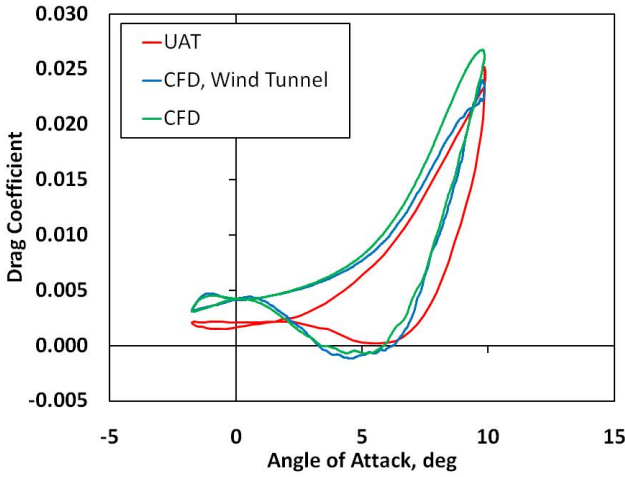
The integrated coefficients for one of the $\alpha_{mean} = 4^\circ$ cases ($\phi = 148^\circ$) are plotted in Fig. 12. The CFD predictions indicate overall good correlation, even when the motion equations rather than digitized flap motion were employed. The experimental data were averaged over 10 cycles of data to produce the mean response. The CFD simulations used a RANS/LES hybrid turbulence method that produces similar cycle-to-cycle variation as vorticity is shed from the system. This behavior is different from CFD simulations that apply RANS turbulence methods, which tend to produce less cycle-dependent results due to the statistical nature of the model. Therefore, the HRLES results need to be averaged to produce a mean response. Ten or more cycles with a three-dimensional grid (also necessary for RANS/LES methods) can be computationally expensive. An alternate method where the data after three cycles is averaged over the final two cycles and smoothed with a moving average has been observed to provide predicted means that are comparable to the much more expensive method. This alternate method has been employed for the results presented in this work.



a) Lift coefficient



b) Pitching moment coefficient



c) Drag coefficient

Figure 12: Dynamic coefficients for the flapped NACA 0012 airfoil for an $\alpha_{mean}=4^\circ$, and a flap phase lag of $\phi=148^\circ$ compared with experimental results [6].

For the $\alpha_{mean} = 4^\circ$ cases, the influence of the wind tunnel walls was observed to be minimal, as illustrated in Fig. 12 by comparing the CFD curves (blue and green). The experimental forces and moments were obtained by integrating over the pressure taps, which may give rise to errors as it may not capture all of the salient features. The CFD results were integrated using the pressure tap locations, as best determined from the figure of the pressure coefficient in Ref. [6]. Lift and moment results indicated little variation from the results

integrated using the entire CFD set of points. Pressure drag integrations resulted in significant differences near the lower end of the angle of attack sweep, which also appeared to be nonphysical. This could be a partial explanation of why the experimental reference [6] does not provide pressure drag information.

The UAT model was trained with the experimental data for lift and moment, and shows excellent correlation with the experimental data, as illustrated by Fig. 12. Given the absence of the experimental pressure drag results, the model was trained using the CFD wind tunnel results for the flapped airfoil. The model shows overall good correlation with the CFD results in Fig. 12, capturing the behavior of the stall, the maximum pressure drag and the cross-over at the low end of the simulation.

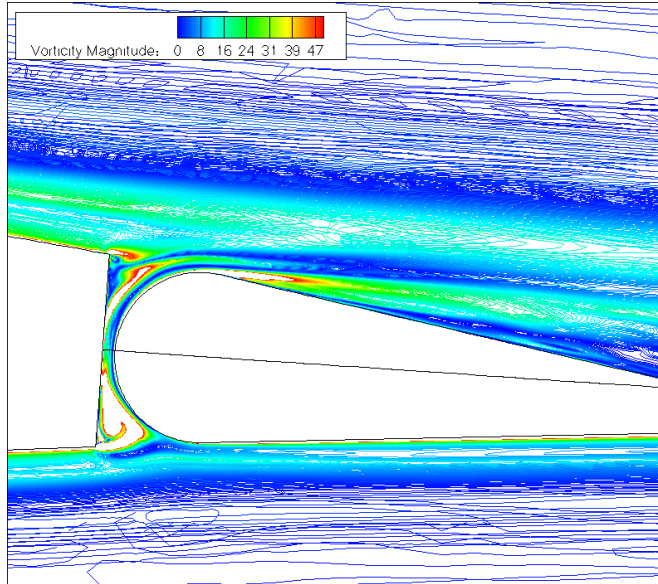
The simulation for the $\alpha_{mean} = 4^\circ$ case with a flap phase lag of $\phi = 206^\circ$ resulted in strong oscillations during the lower portion (about 5°) downstroke of the cycle, unlike the other two flap phase lag cases. The source of these oscillations appears to be additional shedding of vorticity from the flap gap region that is exacerbated by the differential motions during the downstroke. For $\phi = 206^\circ$ phase lag, the flap has reached its maximum upstroke and is reversing direction. This motion generates a vortical shedding along the upper surface of the flap emanating from the gap region that continues during the airfoil downstroke, as observed in Fig. 13.

When the mean airfoil angle of attack (α_{mean}) is increased to 11° , deep dynamic stall is encountered. As with some of the lower mean angles of attack, the flap motion appears to be different than the actual motion as evidenced by the lift correlation, which is typically well-captured with CFD.

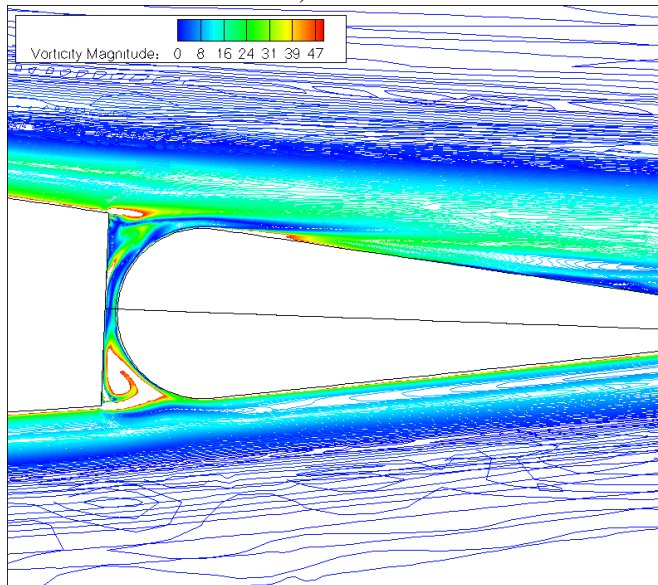
Investigation of the UAT model robustness was verified by training with data from experiment, CFD results of the NACA0012 airfoil, and CFD results of the NACA0012 flapped airfoil. The case with the nominal $\phi=177^\circ$ (actual $\phi=160^\circ$) flap phase lag is discussed here as a representative example of the correlations obtained with CFD and the UAT model, shown in Fig. 14. The UAT model predicts similar results for the lift and moment where all three data sources are available. The UAT recovers the lift more rapidly than the recovery observed in the CFD results at the cycle minimum, and correlates well with the experimental data in this region. The UAT model predicts a cross-over point at 13° , which is within 1° of the location where the experimental data from the upstroke and downstroke come closest for the lift coefficient, and where the moment coefficient has a cross-over. It is speculated that Ref. 6 should actually reflect a cross-over point at this location in the experimental lift coefficient. At the cycle maximum, the UAT does not predict the sharp peak observed in the experiment and CFD, which appears to be an interaction of the vortex shedding and airfoil-flap motion.

The higher than expected lift recovery during the upstroke below the cross-over point observed in the CFD simulations was examined to try and determine its cause. The theoretical model evaluated by Krzysiak and Narkiewicz [6], also showed similar, though not exact behavior. Integration of the coefficients using the estimated pressure tap locations resulted in a 5%-7% decrease of lift coefficient on the upslope, but

could not account for the change in the behavior or the 20%-25% difference with the experimental data. Likewise, simulations without the wind tunnel walls did not provide significant change in the data characteristics. It is also observed (Fig. 10, Ref. 6) that the integrated characteristics from experimental data for these tests were significantly lower at the dynamic stall minimum than integrated characteristics from other dynamic stall campaigns without the flap. This indicates the need for further analysis of the experimental data, as well as the CFD simulations.

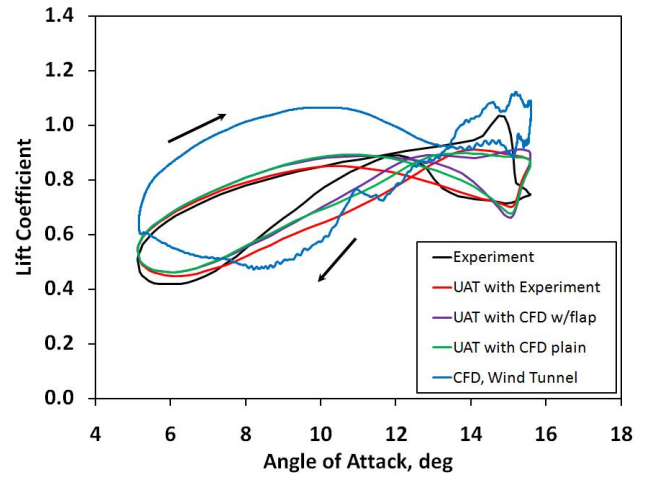


a) $\alpha = 5^\circ$

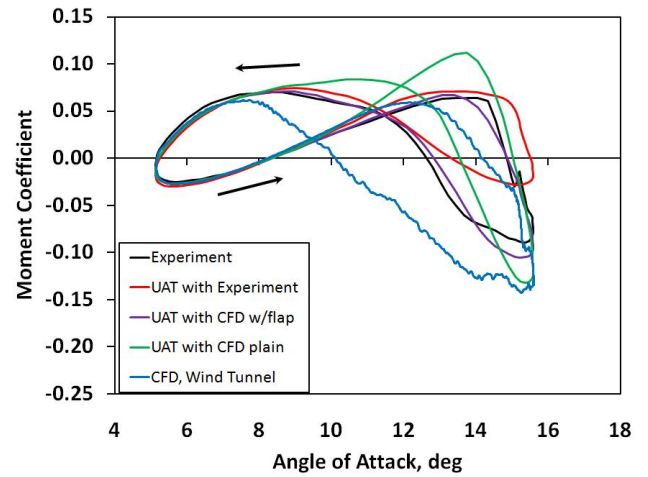


b) $\alpha = 2.15^\circ$

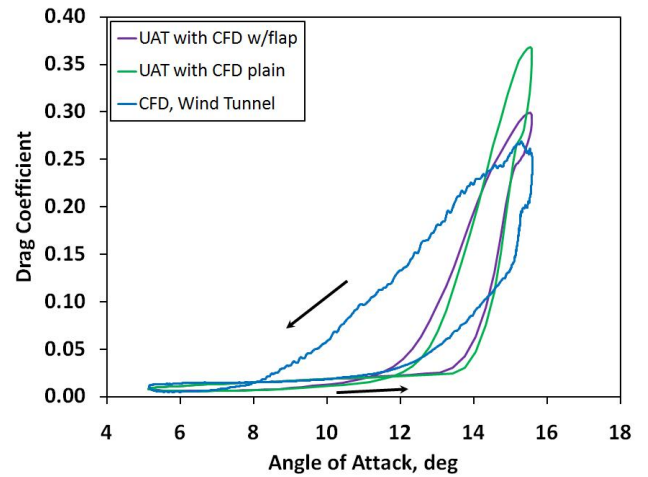
Figure 13: Vortical shedding during the airfoil downstroke for the flapped NACA 0012 airfoil for an $\alpha_{mean}=4^\circ$, and a flap phase lag of $\phi=206^\circ$.



a) Lift coefficient

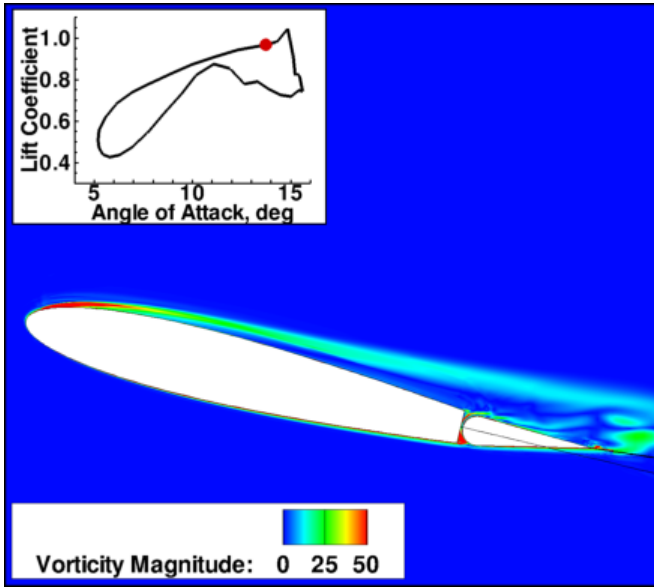


b) Pitching moment coefficient

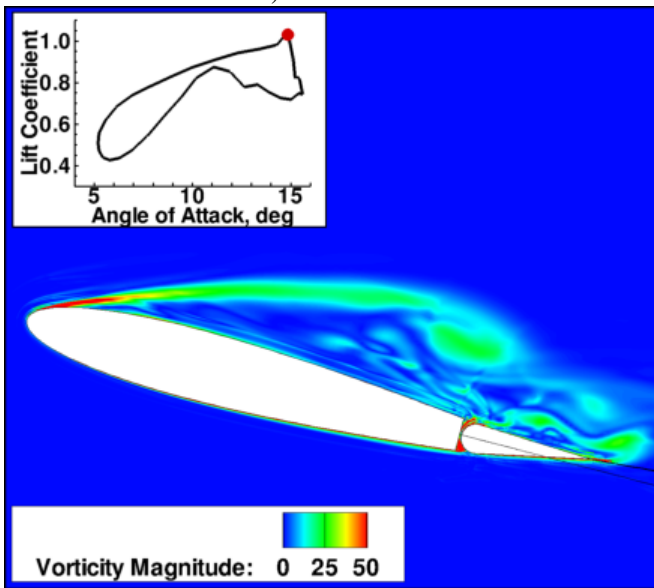


c) Drag coefficient

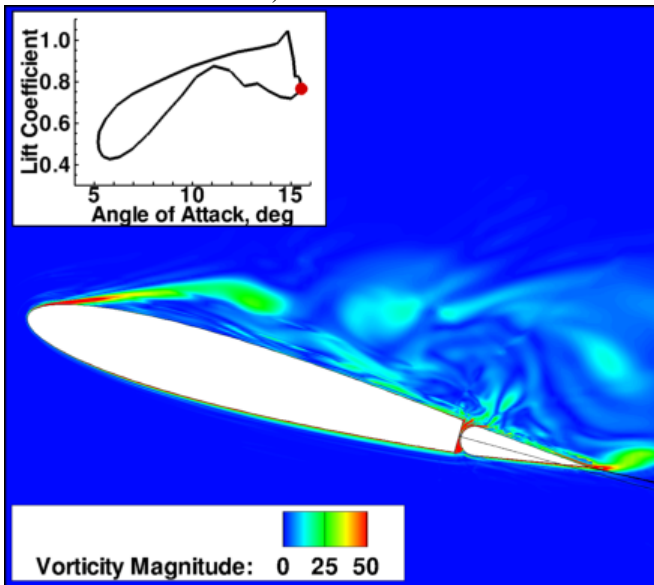
Figure 14: Dynamic coefficients for the flapped NACA 0012 airfoil for an $\alpha_{mean}=11^\circ$, and a flap phase lag of $\phi=177^\circ$ compared with experimental results [6].



a) $\alpha = 13.73^\circ$



b) $\alpha = 14.86^\circ$



c) $\alpha = 15.55^\circ$

Figure 15: Vorticity flowfield for the flapped NACA 0012 airfoil for $\alpha_{mean} = 11^\circ$, and a flap phase lag of $\phi = 177^\circ$.

The consideration of the instantaneous vorticity flowfield (Fig. 15) may provide additional insights into the origin of the sharp lift increase at the cycle maximum. At 13.73° , trailing edge separation just after the shoulder of the flap is apparent, as is separation on the main airfoil at about 25% of the main airfoil chord. As the angle of attack is increased to $\alpha = 14.86^\circ$, the combination of the airfoil and flap motion results in a complex interaction of the vorticity on the upper surface. Strong vorticity is present and is being shed from the flap gap (shown as red contours), resulting in secondary shed vortices from the flap. This vorticity interacts with the main airfoil shed vortex. Although the separation location on the main airfoil is now closer to the leading edge, the large secondary suction peak at the flap leading edge, combined with recirculating flow over the upper surface of the airfoil and flap result in a sharp rise in the integrated lift. As the angle of attack increases to 15.55° , the vorticity from the flap is shed and moves away from the airfoil surface, reducing its interaction with the main airfoil vortex, and resulting in a sharp decrease in lift.

Differences in using the NACA0012 without the flap arise in the moment coefficient prediction, as expected. The influence of the flap motion to mitigate the sharp stall is observed in the region above the cross-over point. Interestingly, the CFD-trained UAT model predicts the moment behavior in stall more closely than the experimentally-trained UAT model.

The drag coefficient predictions by the UAT model trained by the static CFD results match well at the cycle maximum and minimum. Again, the mitigation of the dynamic stall by the flap is readily observed. The poorer correlation between 8° and 14° needs to be further investigated, but this may be attributed to different physics encountered by the CFD simulations, as discussed previously.

CONCLUSIONS

This paper is a first look at using a combination of CFD and the simplified UAT to explore the physics of dynamic stall in single- and multi-element airfoils. Results using the two methods are first compared for a single-element cambered airfoil in dynamic stall (VR-7). The CFD results provide physical insight into the flow physics that result in a double stall behavior. The UAT model captures the overall shape of the dynamic airloads, however it does not have sufficient texture to resolve the double stall peaks. The UAT shows good correlations to the experimental data, regardless of whether experimental static data or CFD static data are used to train the model. Both CFD and UAT give reasonable estimates of drag coefficient.

The approach is further applied to a multi-element symmetric airfoil, a NACA 0012 airfoil with trailing-edge flap. Experimental data for lift and pitching moment are well correlated for $\alpha_{mean}=4^\circ$. In addition, CFD drag data are used to train the UAT to get an estimate of dynamic drag. For the $\alpha_{mean}=11^\circ$ cases, some differences are seen between CFD, UAT, and experimental results. The UAT gives reasonable correlation using a variety of static data inputs, however it does not capture the sharp peak in lift coefficient near the onset of stall. CFD results capture this lift peak, but show a slower recovery during the downstroke. One possible source of this

discrepancy additional errors between the intended airfoil motion compared to the actual deflections.

This work reflects the initial effort in applying CFD in conjunction with UAT to gain physical insight into dynamic stall effects on morphing airfoils. Future work will include additional experimental correlations, further treatment of wind tunnel wall corrections, and evaluation of experimental errors for the NACA0012 flapped airfoil.

ACKNOWLEDGMENTS

This work is sponsored by the National Rotorcraft Technology Center (NTRC) Vertical Lift/Rotorcraft Center of Excellence (VLRCOE) at the Georgia Institute of Technology. Dr. Mike Rutkowski is the technical monitor of this center. Opinions, interpretations, conclusions, and recommendations are those of the authors and are not necessarily endorsed by the United States Government. Computational support was provided by the DoD High Performance Computing Centers at NAVO through an HPC grant from the US Army (S/AAA Dr. Roger Strawn).

References

- [1] L. Ahaus. *An Airloads Theory for Morphing Airfoils in Dynamic Stall with Experimental Correlation*. PhD thesis, Washington University, May 2010.
- [2] L. Ahaus and D. A. Peters. Unified Airloads Model for Morphing Airfoils in Dynamic Stall. In *Proceedings of the 2010 American Helicopter Society Aeromechanics Specialist's Meeting*, San Francisco, CA, January 2010.
- [3] D. Greenwell. Gurney Flaps on Slender and Nonslender Delta Wings. *Journal of Aircraft*, 47(2):675–681, March-April 2010.
- [4] J. Kiedaisch, H. Nagib, and B. Demanett. Active Flow Control Applied to High-Lift Airfoils Utilizing Simple Flaps. In *3rd AIAA Flow Control Conference*, AIAA 2006-2856, San Francisco, CA, June 2006.
- [5] M. Kinzel, M. Maughmer, and E. Duque. Numerical Investigation on the Aerodynamics of Oscillating Airfoils with Deployable Gurney Flaps. *AIAA Journal*, 48(7):1457–1469, July 2010.
- [6] A. Krzysiak and J. Narkiewicz. Aerodynamic Loads on Airfoil with Trailing-Edge Flap Pitching with Different Frequencies. *Journal of Aircraft*, 43(2):407–418, March-April 2006.
- [7] T. Lee and P. Gerontakos. Unsteady Airfoil with Dynamic Leading- and Trailing-Edge Flaps. *Journal of Aircraft*, 46(3):1076–1081, May-June 2009.
- [8] N. Liggett and M. Smith. Cavity Flow Assessment Using Advanced Turbulence Modeling. In *48th AIAA Aerospace Sciences Meeting Including the New Horizons Forum and Aerospace Exposition*, AIAA 2010-1200, Orlando, FL, January 2010.
- [9] J. Little, M. Nishihara, and I. Adamovich. High-Lift Airfoil Trailing Edge Separation Control Using a Single Dielectric Barrier Discharge Plasma Actuator. *Experiments in Fluids*, 48(3):521–537, March 2010.
- [10] L. Liu, A. Padthe, P. Friedmann, E. Quon, and M. Smith. Unsteady Aerodynamics of Flapped Airfoils and Rotors Using CFD and Approximate Methods. In *65th Annual Forum Proceedings - AHS International*, volume 2, pages 1266–1285, 2009.
- [11] K. McAlister, O. Lambert, and D. Petot. Application of the ONERA Model of Dynamic Stall. Technical Report 2399, NASA, 1984.
- [12] W. McCroskey. The Phenomenon of Dynamic Stall. Technical Report 81264, NASA, March 1981.
- [13] W. McCroskey. A Critical Assessment of Wind Tunnel Results for the NACA 0012 Airfoil. Technical Report 100019, NASA, October 1987.
- [14] W. McCroskey, K. McAlister, L. Carr, and S. Pucci. An Experimental Study of Dynamic Stall on Advanced Airfoil Sections Volume 1. Summary of the Experiment," and "Volume 2. Pressure and Force Data. Technical Report 84245, NASA, 1982.
- [15] R. Meyer, W. Hage, D. Bechert, M. Schatz, T. Knacke, and F. Thiele. Separation Control by Self-Activated Movable Flaps. *AIAA Journal*, 45(1):191–199, January 2007.
- [16] M. Moulton and M. Smith. The Prediction and Validation of Static and Dynamic Stall. In *AHS International Meeting on Advanced Rotorcraft Technology and Safety Operations*, Ohmiya, Japan, 2010.
- [17] J. Perraud and F. Moens. Transport Aircraft 3D High Lift Wing Numerical Transition Prediction. In *45th AIAA Aerospace Sciences Meeting and Exhibit*, AIAA 2007-264, Reno, NV, January 2007.
- [18] D. Petot. Progress in the Semi-Empirical Prediction of the Aerodynamic Forces Due to Large Amplitude Oscillations of an Airfoil in Attached or Separated Flow. In *Proceedings of the Ninth European Rotorcraft Forum*, Stresa, Italy, September 1983.
- [19] D. Petot. Differential Equation Modeling of Dynamic Stall. *Rech. Aerosp.*, 5:59–72, 1989.
- [20] M. Sanchez-Rocha. *Wall-Models for Large Eddy Simulation Based on a Generic Additive-Filter Formulation*. PhD thesis, Georgia Institute of Technology, December 2008.
- [21] A. B. Shelton, K. Braman, M. J. Smith, and S. Menon. Improved Turbulence Modeling for Rotorcraft. *submitted to the Journal of the American Helicopter Society*, 2009.
- [22] M. Smith, B. Koukol, T. Quackenbush, and D. Wachspress. Reverse- and Cross-Flow Aerodynamics for High Advance-Ratio Flight. In *35th European Rotorcraft Forum 2009*, volume 1, pages 392–412, 2009.
- [23] Q. Zhang, W. Schroder, and M. Meinke. A Zonal RANS-LES Method to Determine the Flow Over a High-Lift Configuration. *Computers and Fluids*, 39(7):1241–1253, 2010.